NUCL SCI TECH (2017) 28:121
DOI 10.1007/s41365-017-0272-1

A new consecutive energy calibration method for X/γ detectors based on energy continuously tunable laser Compton scattering light source

Hang-Hua Xu[1,2] · Hai-Long Wu[1] · Gong-Tao Fan[1] · Jian-Hui Chen[1] · Dong Wang[1]

Received: 9 March 2017 / Revised: 5 April 2017 / Accepted: 19 April 2017 / Published online: 5 August 2017

Abstract In this paper, we present an energy calibration method based on steep Compton edges of the laser Compton scattered (LCS) photon energy spectra. It performs consecutive energy calibration in the neighborhood of certain energy, hence improves calibration precision in the energy region. It can also achieve direct calibration at high energy region (several MeV) where detectors can only be calibrated by extrapolation in conventional methods. These make it suitable for detectors that need wide-range energy calibration with high precision. The effects of systematic uncertainties on accuracy of this calibration method are studied by simulation, using the design parameters of a LCS device—SINAP III. The results show that the SINAP III device is able to perform energy calibration work over the energy region of 25–740 keV. The precision of calibration is better than 1.6% from 25 to 300 keV and is better than 0.5% from 300 to 740 keV.

Keywords Laser Compton scattering (LCS) · Energy calibration method · Gamma-ray application · Monte Carlo simulation

This work was supported by the National Key Research and Development Program of China (No. 2016YFA0401901) and the National Natural Science Foundation of China (No. 11405427).

✉ Dong Wang
wangdong@sinap.ac.cn

Hang-Hua Xu
xuhanghua@sinap.ac.cn

1 Shanghai Institute of Applied Physics, Chinese Academy of Sciences, Shanghai 201800, China

2 University of Chinese Academy of Sciences, Beijing 100049, China

1 Introduction

With the continuous development of space science, space industry attracts great attentions all over the world. The aerospace X/γ detectors, which are commonly installed on spacecraft, are of great importance in, for example, gamma-ray burst (GRB) observation [1, 2], elemental composition detection of planetary surface [3, 4], black hole investigation [5–7], study of the flare and solar energetic particle (SEP) events [8, 9], nuclear detonation inspection [10] and other fundamental or application researches. All these require the X/γ detectors of high energy resolution in energy region from dozens of keV to several MeV.

At present, radioactive isotopes, such as ^{241}Am, ^{60}Co, ^{137}Cs, ^{40}K and ^{208}Tl, are often used as aerospace X/γ detector calibration sources [11]. However, they provide isolated monoenergetic X/γ-rays and the detectors are calibrated through linear interpolation or extrapolation. This is not suitable for energy calibration over a wide energy region since the linearity of detectors' response would become deteriorated [12–14]. Besides, radioactive isotopes can scarcely produce γ-rays over several MeV [15, 16]. Despite its good energy tunability from the infrared to the X-ray region, synchrotron radiation is not suitable for this task either, because it can hardly reach over 300 keV [17–19]. Bremsstrahlung can produce high energy photons, but its intensity changes slowly over a wide spectral range, making it not suitable for energy calibration [20].

Laser Compton scattering (LCS) γ source is a potential solution to overcome the above difficulties. It uses high-power short-pulse laser beam with high-brightness relativistic electron beam to achieve Compton scattering and

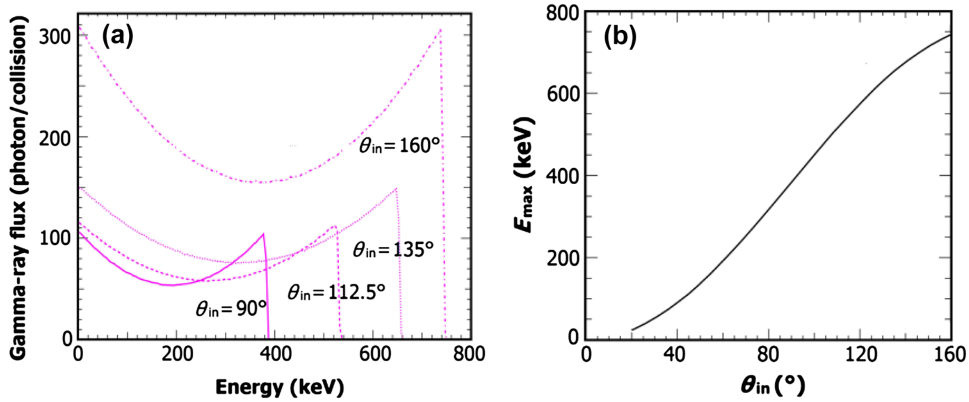

Fig. 1 (Color online) Gamma spectra (**a**), at different laser incident angles, and the $E_{\max} - \theta_{\text{in}}$ relationship (**b**), at $E_e = 180$ MeV and $\lambda = 800$ nm, on SINAP III

produce high-flux, short-pulse, quasi-monochromatic X/γ-ray. The past decades, with advances in accelerator and laser technology, witnessed rapid development of the LCS X/γ-ray source, which is rated as one of the most potential ultra-short-pulse light sources [21]. Currently, LLNL [22], PLS [23], CLS [24], ELI-NP [25], ALBA [26], MIT [27], SPring-8 [28, 29], JAEA [30], SSRF [31, 32], INFN [33], TUNL [34] and other research institutions are committed to the construction of the experimental devices of LCS.

With an energy-calibrated high-purity germanium (HPGe) detector, the exact energy and shape of the high energy edge of the measured Compton spectrum were used to determine the electron energy and the electron beam energy spread in BESSY I [35]. Sun et al. improved this beam diagnostics method with a more comprehensive model and successfully determined the electron beam energy of the HIGS's storage ring [36, 37]. This technique can be applied to detector energy calibration with the electron beam of known energy, i.e., using a series of Compton edges of the X/γ-ray spectra produced by LCS to calibrate the detectors. Recently, at NewSUBARU, Hiroaki et al. attempted with a similar idea and calibrated $LaBr_3(Ce)$ detector at 10.19, 9.14 and 8.19 MeV with LCS edges by changing the electron beam energy [14].

The proposed SINAP III [38, 39] facility is such a kind of LCS γ source: by changing continuously the colliding angle between the electron beam and laser beam, the steep Compton edge of scattered photon energy spectrum is thus continuously adjustable from 25 to 740 keV. In this paper, we present an energy calibration method developed to perform consecutive calibration over a wide energy region based on this facility.

In this article, the principle of consecutive energy calibration method and the calibration steps are introduced. The process to precisely determine location of the Compton edge is described in detail. The simulation setups to study the dependence of the calibration accuracy on relevant systematic uncertainties are demonstrated. The simulation results and the calibration accuracy are discussed. Finally, we summarize this consecutive detector energy calibration method and propose the future application of this method on other LCS facilities.

2 Principle of consecutive detector energy calibration based on LCS

For relativistic electron, energy expressions of γ-ray generated from laser electron Compton scattering [31, 40] are as follows:

$$E_\gamma = \frac{E_{\text{L}}(1-\beta\cos\theta_{\text{in}})}{(1-\beta\cos\theta)+\frac{E_{\text{L}}}{E_e}\gamma^2(1-\beta)(1+\cos\theta)(1-\beta\cos\theta_{\text{in}})} \tag{1}$$

where E_{L} and E_e are the incident photon and electron energy, respectively, in laboratory reference frame; θ_{in} is the angle between the incident laser and electron movement direction, referred to as the laser incident angle; and θ is the angle between the direction of movement of the scattered photons and electrons, referred to as the γ-ray scattering angle. When θ_{in}, E_{L}, E_{e} are fixed, E_γ reaches the theoretical maximum value $E_{\max}$ when $\theta = 0$.

$$E_{\max} = \frac{\gamma^2 E_{\text{L}} E_e(1+\beta)(1-\beta\cos\theta_{\text{in}})}{E_e + 2\gamma^2 E_{\text{L}}(1-\beta\cos\theta_{\text{in}})} \tag{2}$$

Energy spectrum of Compton scattering drops rapidly at $E_{\max}$, generating a steep Compton edge. According to Eq. (2), when E_{L}, E_e are fixed, $E_{\max}$ and θ_{in} is one-to-one corresponded [41]. SINAP III is designed based on this principle. The simulated γ spectra of different laser incident angles θ_{in} generated by SINAP III are shown in Fig. 1a. The $E_{\max} - \theta_{\text{in}}$ relationship is shown in Fig. 1b.

Thus, a consecutive energy calibration method based on the Compton edge can be carried out in following steps,

(1) Measure the LCS energy spectrum at a laser incident angle $\theta_{\text{in}-i}$ to obtain the $E_{\max}(i)$ by Eq. (2);

(2) Find the Compton edge channel address, i.e., Channel#(i);
(3) Change θ_{in} and repeat steps (1) and (2);
(4) With the array of [Channel#(i), $E_{\max}(i)$] occupied, a map between channel address and $E_{\max}$ can be generated, corresponding to a series of points on the plane where the channel address is the x coordinate and the γ-ray energy is the y coordinate. Finish the calibration by fitting the points with a polynomial equation just like what calibration is done in conventional way [11].

The advantage of this consecutive energy calibration method is that the points can be generated over a wide range of energy with very small intervals. On SINAP III, we can generate a series of Compton edges in energy steps of no larger than 0.07 keV by changing incident laser angle θ_{in} with 0.01°. This enables the calibration of a specific range near any particular energy of interest with tiny rotation of the incident laser and avoids the error brought by the extrapolation from full energy peaks of radioactive isotopes. The experimental steps of switching various radioactive isotope sources can also be omitted which would make the calibration process more compact, safe and easy to be automated.

3 Determination of the Compton edge location

In the above calibration steps, the key issue of this method is how to determine the channel address of the Compton edge $E_{\max}$ precisely. In actual situation, the systematic uncertainties or variables, such as energy spread $\Delta E/E$ and the emittance of electron bunches ε, would smear the Compton edge (Fig. 2). Fortunately, as will be discussed later in Sect. 4, the corresponded energy at midpoint of the edge is quite stable if the systematic uncertainties do not vary too much during the calibration, and is approximately equal to $E_{\max}$, with a difference of <1.6% (denoted as $\Delta E_{\max}$).

So, the key to this method now turns into finding the midpoint of Compton edge E_{mid} or channel number C_{mid} (E_{mid} and C_{mid} are equivalent in this scenario, and we will always use E_{mid} from now on) which is approximate enough to $E_{\max}$. Two fitting methods are applied to the simulated energy spectra. The fitting function derived in Refs. [35, 36] is also applied as comparison. The results show that all the three methods can solve the problem with satisfactory accuracy.

The linear fitting method is of five steps:

(1) Find the channel C_{peak} with the highest count N_{peak} in the spectrum. Start from C_{peak} and search toward the right side of C_{peak}, and stop at the first channel C_{low} where the count is less than $20\%N_{\mathrm{peak}}$.
(2) Choose the low platform (P_{L}) of the energy spectrum near the Compton edge. The P_{L} is in width of k_{L} channels, with C_{low} being the initial left endpoint and N_{L} being the platform height averaged from the counts of the k_{L} channels. Move the platform one channel toward the right side and calculate N_{L} again, denoted as N_{L}'. If $|N_{\mathrm{L}} - N_{\mathrm{L}}'| > 0.01N_{\mathrm{L}}$, i.e., if the platform is not well chosen, keep on moving the platform toward the right side channel by channel until $|N_{\mathrm{L}} - N_{\mathrm{L}}'| < 0.01N_{\mathrm{L}}$. Then, the left and right endpoints of the final low platform are denoted as C_{downL} and C_{downR}, respectively.
(3) Choose the high platform (P_{H}) of the energy spectrum near the Compton edge. Start from C_{low} and search toward the left side of C_{low}, and stop at the first channel C_{high} whose count is larger than $80\%N_{\mathrm{peak}}$. The P_{H} is in width of k_{H} channels, with C_{high} being the initial right endpoint and N_{H} being the platform height averaged from the counts of the k_{H} channels. Move the platform one channel toward the left side and calculate N_{H} again, denoted as N_{H}'. If $|N_{\mathrm{H}} - N_{\mathrm{H}}'| > 0.001N_{\mathrm{H}}$, and keep on moving the platform toward the left side channel by channel

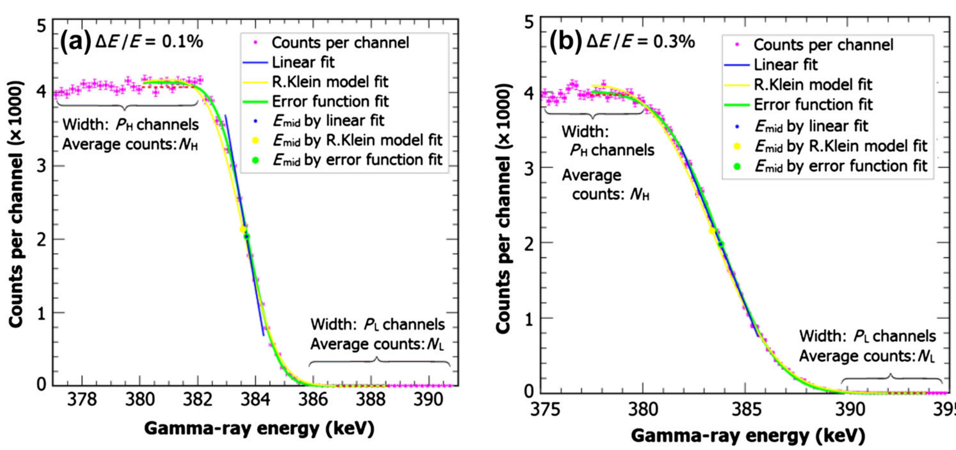

Fig. 2 (Color online) Simulated energy spectra near the Compton edge, at laser wavelength of $\lambda = 800$ nm in collision angle of $\theta_{\mathrm{in}} = 90°$, and electron beam energy of $E_e = 180$ MeV in beam bunch emittance of $\varepsilon = 6$ mm·mrad with energy spread of $\Delta E/E = 0.1\%$ (**a**) and $\Delta E/E = 0.3\%$ (**b**)

until $|N_H - N_H'| < 0.001N_H$. Then, the left and right endpoints of the final chosen high platform are denoted as C_{upL} and C_{upR}, respectively.

(4) Perform a linear fitting to the intercepted energy spectrum between C_{high} and C_{low}

$$C = p_1 N + p_0. \tag{3}$$

(5) Substitute N with $N_{mid} = 50\%N_H + 50\%N_L$ to obtain E_{mid}:

$$E_{mid} = p_1(50\%N_H + 50\%N_L) + p_0. \tag{4}$$

The R. Klein model method is:

$$N(E_\gamma, a_1, a_2, a_3, a_4, a_5) = a_3\left\{\frac{1}{2}\left[1 + a_4(E_\gamma - a_1)\right]erfc\left(\frac{E_\gamma - a_1}{\sqrt{2}a_2}\right) - \frac{a_2 a_4}{\sqrt{2\pi}}\exp\left(-\frac{(E_\gamma - a_1)^2}{2a_2^2}\right)\right\} + a_5. \tag{5}$$

where a_1–a_5 are the coefficients to be determined. Here, a_1 corresponds to E_{mid}. Another fitting model in Ref. [36] is not applied as we neglect the collimation effect yet. The fitting range is the intercepted energy spectrum between C_{upL} to C_{downR}.

The error function method is:

$$N = C_0 - C_1 \mathrm{erf}(C/\sigma - E_{mid}/\sigma), \tag{6}$$

where erf is the standard error function, C_0, C_1, E_{mid} and σ are the coefficients to be determined. This one is equivalent to the fitting function used in Ref. [42] and can be regarded as a simplified model of Eq. (5) with $a_4 = 0$.

4 Simulation setup

The energy calibration method is tested with the data generated by an updated 4D Monte Carlo simulation code [43]. Main parameters of the laser and electron beams of SINAP III for the simulation are listed in Table 1.

Ten system variables affecting the γ-ray spectrum are listed in Table 2, where the input value of each variable changes within its scan range, so that ΔE_{max} caused by systematic uncertainties of SINAP III can be simulated.

5 Results and discussion

We will first demonstrate a rough estimation of ΔE_{max} at a certain incident angle, and then extend it to the whole adjustable angle range of SINAP III, i.e., [20°, 160°]. Finally, consider the deviation correction and give a more accurate ΔE_{max}.

Table 1 Main parameters of the laser and electron beams for the SINAP III simulation

Parameters	Value
Electron energy (MeV)	180
Energy spread	0.1%
Emittance (mm mrad)	6
Bunch length (rms) (mm)	$\sigma_{le} = 0.72$
RMS beam size (μm)	$\sigma_{we} = \sigma_{he} = 20$
Laser wavelength (nm)	800
Energy/pulse (mJ)	1.75
Repetition rate (Hz)	1000
Pulse length (rms) (ps)	$\sigma_{lp} = 1$
RMS beam size (μm)	$\sigma_{wp} = \sigma_{hp} = 20$
Incident angle (°)	20, 45, 67.5, 90, 112.5, 135, 160

Table 2 Scan range of the system variables

System variables	Scan range
Laser incident angle θ_{in} (°)	$[\theta_C - 0.05, \theta_C + 0.05]$[a]
Laser wavelength λ (nm)	[797.5, 802.5]
The center value of electron energy E_e (MeV)	[179.9, 180.1]
Emittance ε (mm·mrad)	[5, 32]
Electron energy spread $\Delta E/E$	[0.0005,0.0055]
Spot size of laser waist σ_l (μm)	[20,70]
RMS beam size of electron σ_e (μm)	[20,70] ($\sigma_e = \sigma_{we} = \sigma_{he}$)
Deviation between laser pulse center and electron bunch in horizontal (D_x),vertical (D_y) and electron beam (D_z) directions	D_x(μm): [−50,50] D_y(μm):[−50,50] D_z(mm): [−1.5,1.5]

[a] θ_C is the center value of the scan range of the laser incident angle. It changes every time the simulation loops over all the other input settings. $\theta_c \in [20°, 160°]$

5.1 Estimation of ΔE_{max} at a certain incident angle

Let us demonstrate the calculation process in which laser incident angle is 90° as an example. All the system variables are set equal to the center values at the beginning. In order to evaluate the deviation between E_{max} and E_{mid} caused by the variation of one particular system variable q, which is denoted as ΔE^q_{max}, the scanned range of the concerned system variable is evenly divided into $(m-1)$ intervals. Then the input value of the concerned system variable in the simulation will switch through the m endpoints of the intervals while the other system variables remain unchanged. Next, apply the three fitting methods mentioned in the previous section to the simulation data to get E_{mid}. Finally, we obtained ΔE_{max} which is defined as the average deviation between $E_{\max}$ and E_{mid} of the m samples.

$$\Delta E_{\max}^{q} = \overline{|E_{\text{mid}}(q_i) - E_{\max}(q_i)| + err_{E_{\text{mid}}}(q_i)} = \frac{1}{m}\sum_{i=1}^{m}\left[|E_{\text{mid}}(q_i) - E_{\max}(q_i)| + err_{E_{\text{mid}}}(q_i)\right] \quad (7)$$

where $q\in(\varepsilon,\ \Delta E/E,\ \sigma_1,\ \sigma_e,\ D_x,\ D_y,\ D_z,\ \theta_{\text{in}},\ \lambda,\ E_e)$ and $err_{E\text{mid}}(q_i)$ is the fitting error of $E_{\text{mid}}(q_i)$.

Repeat the above steps through every system variable, the $\Delta E_{\max}^{q}$ caused by 10 system variables are collected and the $\delta\Delta E_{\max}^{q} = \Delta E_{\max}^{q}/E_{max}$ is calculated. The results are given in Table 3.

The total error $\Delta E_{\max}$ and relative error $\delta E_{\max}$ can now be represented as the following equations,

$$\Delta E_{\max} = \sqrt{\sum_{q}\Delta E_{\max}^{q}},\quad \delta E_{\max} = \sqrt{\sum_{q}\delta E_{\max}^{q}} \quad (8)$$

The values of $\delta\Delta E_{\max}^{q}$ in Table 3 are all less than 0.05%, so $\delta E_{\max}|_{\theta\text{c}=90°} < 10^{1/2} \times 0.05 = 0.16\%$, which infers that E_{mid} coincide well with $E_{\max}$ at $\theta_{\text{C}} = 90°$.

5.2 Estimation of $\Delta E_{\max}$ from 20° to 160°

In order to test whether E_{mid} is always consistent with $E_{\max}$ in the other cases, the operations are repeated at $\theta_{\text{in}} = 20°-160°$. As shown in Fig. 3, the $\delta E_{\max}$ values are less than 1.6%, with the same scan ranges of systematic uncertainties as in $\theta_{\text{in}} = 90°$.

5.3 Deviation correction

The above $\Delta E_{\max}$ and $\delta E_{\max}$ need correction because $E_{\max}(q_i)$ in Eq. (7) changes when different θ_{in}, λ and E_e are sampled due to Eq. (2). Take the deviation of $E_{\max}(q_i)$ into consideration, a more precise $\Delta E_{\max}$ expression can be obtained as:

$$\Delta E_{\max} = \sqrt{\sum_{q_{im}}\left(\Delta E_{\max}^{q_{im}}\right)^2 + \sum_{q_{\text{ex}}}\left[\left(\Delta E_{\max}^{q_{\text{ex}}}\right)^2 + \left(|\partial E_{\max}/\partial q_{\text{ex}}|\Delta q_{\text{ex}}\right)^2\right]},$$
$$\delta E_{\max} = \sqrt{\sum_{q_{im}}\left(\delta E_{\max}^{q_{im}}\right)^2 + \sum_{q_{\text{ex}}}\left[\left(\delta E_{\max}^{q_{\text{ex}}}\right)^2 + \left(|\partial E_{\max}/\partial q_{\text{ex}}|\frac{\Delta q_{\text{ex}}}{E_{\max}}\right)^2\right]} \quad (9)$$

where q_{ex} denotes the explicit variables of θ_{in}, λ and E_e, q_{im} denotes the other implicit variables regarding $E_{\max}$, and $\partial E_{\max}/\partial q_{\text{ex}}$ is the partial derivative of $E_{\max}$ with respect to q_{ex}, as shown in Fig. 4.

It is worth mentioning that at $\theta_{\text{in}} = 160°$ we can estimate the following rates from Fig. 5b, c,

Table 3 $\Delta E_{\max}^{q}$ and $\delta\Delta E_{\max}^{q}$ of the three calibration methods at $\theta_{\text{in}} = 90°$

System variables	Center value	Scan range	Linear fit method		Error function method		R. Klein model	
			$\delta\Delta E_{\max}^{q}$/eV	$\delta\Delta E_{\max}^{q}/\times 10^{-5}$	$\Delta E_{\max}^{q}$/eV	$\delta\Delta E_{\max}^{q}/\times 10^{-5}$	$\delta\Delta E_{\max}^{q}$/eV	$\delta\Delta E_{\max}^{q}/\times 10^{-5}$
E (mm·mrad)	6	[5, 32]	44.7	11.6	107.4	28.0	55.1	14.4
$\Delta E/E$	0.001	[0.0005, 0.0055]	125.4	32.7	65.7	17.1	146.5	38.2
σ_l (μm)	20	[20, 70]	20.1	5.23	31.4	8.17	25.6	6.68
σ_e (μm)	20	[20, 70]	30.2	7.88	46.7	12.2	46.4	12.1
D_x (μm)	0	[− 50, 50]	20.2	5.27	29.5	7.70	30.8	8.01
D_y (μm)	0	[− 50, 50]	29.2	7.61	54.3	14.1	55.7	14.5
D_z (mm)	0	[− 1.5, 1.5]	28.0	7.31	62.6	16.3	63.5	16.6
θ_{in} (°)	90	[89.95, 90.05]	19.8	5.17	31.7	8.25	32.8	8.54
λ (nm)	800	[797.5, 802.5]	20.5	5.35	32.7	8.53	32.7	8.52
E_e (MeV)	180	[179.9, 180.1]	19.4	5.06	32.1	8.36	34.2	8.92

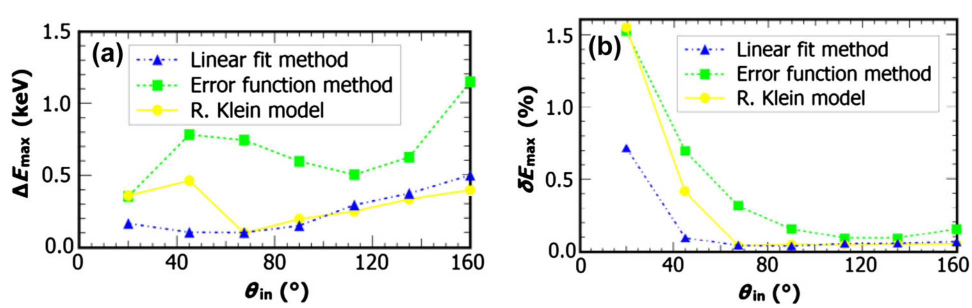

Fig. 3 (Color online) Relationship between $\Delta E_{\max}$ ($\delta E_{\max}$) and θ_{in}

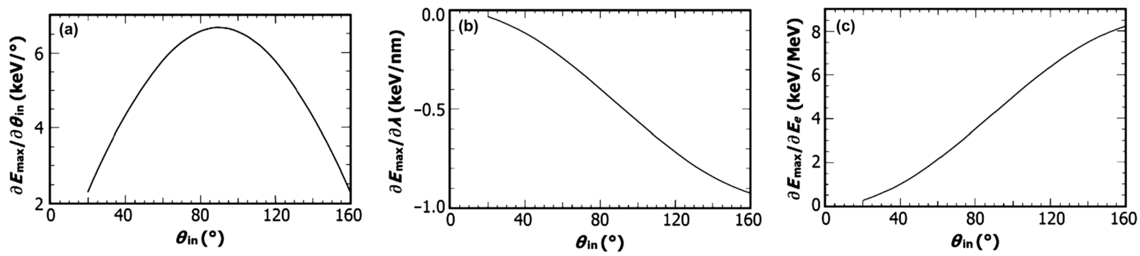

Fig. 4 Partial derivatives of $\partial E_{max}/\partial\theta_{in}$, $\partial E_{max}/\partial\lambda$ and $\partial E_{max}/\partial E_e$ as a function of $\theta_{in} = 20°–160°$ on SINAP III

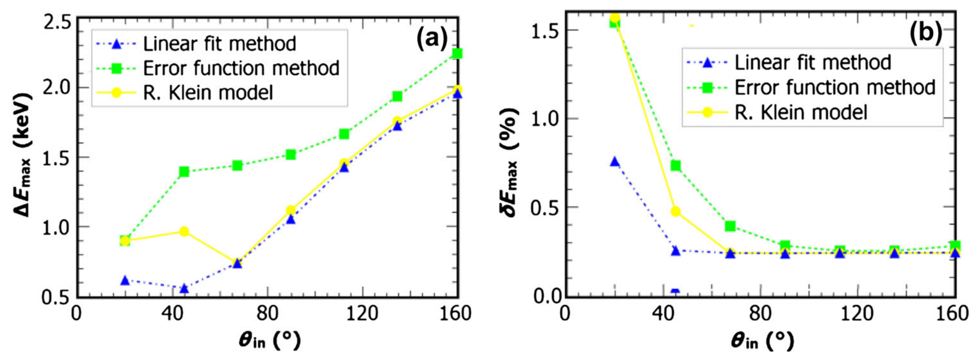

Fig. 5 (Color online) ΔE_{max} and δE_{max} as a function of θ_{in} after correction

$$\frac{\Delta E_{max}/E_{max}}{\Delta\lambda/\lambda} \approx \frac{(\delta E_{max}/\delta\lambda)\lambda}{E_{max}} = \frac{-1\times 800}{740} \approx -1,$$
$$\frac{\Delta E_{max}/E_{max}}{\Delta E_e/E_e} \approx \frac{(\delta E_{max}/\delta E_e)E_e}{E_{max}} = \frac{8\times 180}{740} \approx 2 \qquad (10)$$

The two rates are consistent with the equation $\delta E_{ma}/\Delta E_{max} \approx [(2\sigma_{Ee}/E_e)^2 + (\sigma_{Ep}/E_p)^2]^{1/2}$ derived under head-on ($\theta_{in} = 180°$) LCS geometry [36]. According to design of the SINAP III, typical values of $\delta E_e = 0.1\%$, $\Delta\lambda = 1$ nm and $\Delta\theta_{in} = 0.01°$ are used. The ΔE_{max} and δE_{max} after correction are shown in Fig. 5.

Compared with Fig. 3, we can see that when the laser incident angle θ_{in} gets larger, δE_e and $\Delta\lambda$ contribute more to ΔE_{max} and δE_{max}. In fact, the two systematic uncertainties are almost dominating when $\theta_{in} > 60°$. Over all, the δE_{max} is lower than 1.6% in the energy region of 25–300 keV, lower than 0.5% in the energy region of 300–740 keV, when the systematic uncertainties can be limited within the scan range in the calibration process.

6 Summary

More precise calibration of X/γ detectors in a wide energy range demands new tunable X/γ sources and new calibration methods. LCS light source is a suitable γ source candidate. Continuously changing the collision angle between laser and electron beam is one of the most effective ways to continuously change γ energy spectra's high energy edges [44]. It takes advantage of the one-to-one correspondence of the laser–electron collision angle and the energy of the generated gamma spectrum's Compton edge. In this work, an energy calibration method based on this technique is carried out. It can perform consecutive energy calibration with small energy gap in the neighborhood of a specific energy. This would eliminate the error from extrapolation, solve the problem of the deterioration of detector's linearity and improve calibration accuracy. The uncertainty of this method for the X/γ detectors on SINAP III facility is tested, which is lower than 1.6% in the energy region of 25–300 keV, and is lower than 0.5% in the energy region of 300–740 keV.

This energy calibration method could also be applied on the other LCS light sources with continuously variable laser incident angle. SINAP III is the prototype of the Shanghai Laser Electron Gamma Source [31, 32, 45–47] (SLEGS) on the storage ring of SSRF [48]. Once constructed, the larger energy region and higher repetition rates with lower systematic uncertainties of SLEGS will enable a faster and more precise energy calibration process for X/γ detectors.

Acknowledgements The authors would like to thank Professors Yu-Gang Ma, Hong-Wei Wang and Xing-Tao Wang for helpful discussions.

References

1. Y. Dong, B. Wu, Y. Li et al., SVOM gamma-ray monitor. Sci. Chin. Phys. Mech. Astron. **53**(1), 40–42 (2010). doi:10.1007/s11433-010-0011-7
2. M. Ackermann, M. Ajello, K. Asano et al., Detection of a spectral break in the extra hard component of GRB 090926a. Astrophys. J. **729**(2), 114 (2011). doi:10.1088/0004-637X/729/2/114
3. P.N. Peplowski, L.G. Evans, S.A. Hauck et al., Radioactive elements on mercury's surface from MESSENGER: implications for the planet's formation and evolution. Science **333**(6051), 1850–1852 (2011). doi:10.1126/science.1211576
4. D. Lawrence, M. Burks, D. Do et al. The GeMini plus high-purity Ge gamma-ray spectrometer: Instrument overview and science applications. The 48th Lunar and Planetary Science Conference, (The Woodlands, Texas, 2017), https://www.hou.usra.edu/meetings/lpsc2017/pdf/2234.pdf
5. E.H. Morgan, R.A. Remillard, J. Greiner, RXTE observations of QPOs in the black hole candidate GRS 1915 + 105. Astrophys J **482**(2), 993 (1997). doi:10.1086/304191
6. J.S. Gregory, E.M. Jeffrey, A.R. Ronald et al., Complete RXTE spectral observations of the black hole X-ray nova XTE j1550–564. Astrophys J **544**(2), 993 (2000). doi:10.1086/317229
7. R.A. Remillard, J.E. McClintock, X-ray properties of black-hole binaries. Ann. Rev. Astron. Astrophys. **44**(1), 49–92 (2006). doi:10.1146/annurev.astro.44.051905.092532
8. M. Yoshimori, K. Suga, K. Morimoto et al., Gamma-ray spectral observations with Yohkoh. Int. Astron. Union Colloq. **142**, 639–643 (1994). doi:10.1017/S0252921100077915
9. G.H. Share, R.J. Murphy, A.J. Tylka et al., Gamma-ray line observations of the 2000 July 14 flare and SEP impact on the earth. Sol. Phys. **204**(1), 41–53 (2001). doi:10.1023/a:1014297617919
10. S. Singer, The Vela satellite program for detection of high-altitude nuclear detonations. Proc. IEEE **53**(12), 1935–1948 (1965). doi:10.1109/PROC.1965.4470
11. R. Casanovas, J.J. Morant, M. Salvadó, Energy and resolution calibration of NaI(TI) and $LaBr_3$(Ce) scintillators and validation of an EGS5 Monte Carlo user code for efficiency calculations. Nucl. Instrum. Methods Phys. A **675**, 78–83 (2012). doi:10.1016/j.nima.2012.02.006
12. F. Quarati, A.J.J. Bos, S. Brandenburg et al., X-ray and gamma-ray response of a 2″ × 2″ $LaBr_3$: Ce scintillation detector. Nucl. Instrum. Methods Phys. A **574**(1), 115–120 (2007). doi:10.1016/j.nima.2007.01.161
13. M. Ciemała, D. Balabanski, M. Csatlós et al., Measurements of high-energy-rays with $LaBr_3$:Ce detectors. Nucl. Instrum. Methods Phys. A **608**(1), 76–79 (2009). doi:10.1016/j.nima.2009.06.019
14. H. Utsunomiya, T. Shima, K. Takahisa et al., Energy calibration of the NewSUBARU storage ring for laser Compton-scattering gamma-rays and applications. IEEE Trans. Nucl. Sci. **61**(3), 1252–1258 (2014). doi:10.1109/TNS.2014.2312323
15. R.C. Greenwood, R.G. Helmer, R.J. Gehrke, Precise γ-ray energies for calibration of Ge semiconductor spectrometers to 3.5 MeV. Nucl. Instrum. Methods **159**(2), 465–482 (1979). doi:10.1016/0029-554X(79)90675-X
16. R.G. Helmer, C.V.D. Leun, Recommended standards for γ-ray energy calibration. Nucl. Instrum. Methods Phys. A **422**(1), 525–531 (1999). doi:10.1016/S0168-9002(98)01079-1
17. K. Sun, R. Yi, S. Jiang et al., Calibration of soft X-ray detection with synchrotron radiation. High Energy Phys. Nucl. Phys. **28**(2), 205–209 (2004). doi:10.3321/j.issn:0254-3052.2004.02.020
18. F.V. Hartemann, W.J. Brown, D.J. Gibson et al., High-energy scaling of Compton scattering light sources. Phys. Rev. Spec Top. Accel. Beams **8**(10), 100702 (2005). doi:10.1103/PhysRevSTAB.8.100702
19. W. Eberhardt, Synchrotron radiation: a continuing revolution in X-ray science—diffraction limited storage rings and beyond. J. Electron. Spectrosc. Relat. Phenom. **200**, 31–39 (2015). doi:10.1016/j.elspec.2015.06.009
20. A. Döpp, E. Guillaume, C. Thaury et al., A bremsstrahlung gamma-ray source based on stable ionization injection of electrons into a laser wakefield accelerator. Nucl. Instrum. Methods Phys. A **830**, 515–519 (2016). doi:10.1016/j.nima.2016.01.086
21. P. Eisenberger, S. Suckewer, Subpicosecond X-ray pulses. Science **274**(5285), 201 (1996). doi:10.1126/science.274.5285.201
22. D.J. Gibson, S.G. Anderson, C.P.J. Barty et al., PLEIADES: a picosecond Compton scattering X-ray source for advanced backlighting and time-resolved material studies. Phys. Plasmas **11**(5), 2857–2864 (2004). doi:10.1063/1.1646160
23. J.K. Ahn, E.S. Kim, Design study of the Compton backscattering photon beam facility at the Pohang light source. Nucl. Instrum. Methods Phys. A **528**(1–2), 600–604 (2004). doi:10.1016/j.nima.2004.04.110
24. W.A. Wurtz, Considerations for the construction of a gamma-ray beamline at the Canadian Light Source. (2010). http://physics.usask.ca/~chang/department/Wurtz.pdf
25. D. Habs, T. Tajima, V. Zamfir, Extreme light infrastructure–nuclear physics (ELI–NP): new horizons for photon physics in Europe. Nucl. Phys. News **21**(1), 23–29 (2011). doi:10.1080/10619127.2010.529741
26. J.L. Tain, A.M. Lallena, Proposal for the construction of a gamma-ray beam line at the Spanish Synchrotron ALBA. Consorcio para la construcción, equipamiento y explotación del laboratorio de luz sincrotrón CELLS-ALBA (2004). https://intranet.cells.es/static/Gamma_rays.pdf
27. W.S. Graves, J. Bessuille, P. Brown et al., Compact X-ray source based on burst-mode inverse Compton scattering at 100 kHz. Phys. Rev. Spec. Topics Accel. Beams **17**(12), 120701 (2014). doi:10.1103/PhysRevSTAB.17.120701
28. M. Niiyama, Recent results from LEPS and prospects of LEPS II at SPring-8. Nucl. Phys. A **914**, 543–552 (2013). doi:10.1016/j.nuclphysa.2013.03.013
29. N. Muramatsu, Y. Kon, S. Daté et al., Development of high intensity laser-electron photon beams up to 2.9 GeV at the SPring-8 LEPS beamline. Nucl. Instrum. Methods Phys. A **737**, 184–194 (2014). doi:10.1016/j.nima.2013.11.039
30. R. Hajima, I. Daito, H. Ohgaki et al., Generation of laser Compton scattered gamma-rays from a 150 MeV microtron. In: Proceedings IPAC, vol. 3645 (Shanghai, China, 2013). https://accelconf.web.cern.ch/AccelConf/IPAC2013/papers/thpwa009.pdf
31. Q.Y. Pan, W. Xu, J.G. Chen et al., Shanghai laser electron gamma source (SLEGS). Nucl. Phys. Rev. **25**(2), 129–134 (2008). http://www.npr.ac.cn/EN/Y2008/V25/I2/129
32. Q.Y. Pan, W. Xu, W. Luo et al., A future laser Compton scattering (LCS) γ-ray source: SLEGS at SSRF. Synchrotron Radiat. News **22**(3), 11–20 (2009). doi:10.1080/08940880902959759
33. D. Alesini, I. Chaikovska, S. Guiducci et al., DAΦNE γ-rays factory. IEEE Trans. Nucl. Sci. **63**(2), 913–920 (2016). doi:10.1109/TNS.2015.2488487
34. H.R. Weller, M.W. Ahmed, H. Gao et al., Research opportunities at the upgraded HIGS facility. Prog. Part. Nucl. Phys. **62**(1), 257–303 (2009). doi:10.1016/j.ppnp.2008.07.001
35. R. Klein, T. Mayer, P. Kuske et al., Beam diagnostics at the BESSY I electron storage ring with Compton backscattered laser photons: measurement of the electron energy and related quantities. Nucl. Instrum. Methods Phys. A **384**(2), 293–298 (1997). doi:10.1016/S0168-9002(96)00899-6
36. C. Sun, J. Li, G. Rusev et al., Energy and energy spread measurements of an electron beam by Compton scattering method.

Phys. Rev. Special Top. Accel. Beams **12**(6), 062801 (2009). doi:10.1103/PhysRevSTAB.12.062801

37. C. Sun, Dissertation characterizations and diagnostics of Compton light source. Place Published: Duke University, 2009. http://hdl.handle.net/10161/1579
38. W. Xu, W. Luo, B.S. Huang et al., Adjustable LCS γ source SINAP-III. Nucl. Phys. Rev. **29**(3), 253–258 (2012). doi:10.11804/NuclPhysRev.29.03.253
39. H. Xu, G. Fan, H. Wu et al., Interaction chamber design for an energy continuously tunable sub-MeV laser-Compton gamma-ray source. IEEE Trans. Nucl. Sci. **63**(2), 906–912 (2016). doi:10.1109/TNS.2015.2496256
40. W. Luo, W. Xu, Q.Y. Pan et al., A laser-Compton scattering prototype experiment at 100 MeV linac of Shanghai Institute of applied physics. Rev. Sci. Instrum. **81**(1), 013304 (2010). doi:10.1063/1.3282445
41. Y. Taira, M. Adachi, H. Zen et al., Generation of energy-tunable and ultra-short-pulse gamma-rays via inverse Compton scattering in an electron storage ring. Nucl. Instrum. Methods Phys. A **652**(1), 696–700 (2011). doi:10.1016/j.nima.2010.08.036
42. H. Zen, Y. Taira, T. Konomi et al., Generation of high energy gamma-ray by laser Compton scattering of 1.94-µm fiber laser in UVSOR-III electron storage ring. Energy Proced. **89**, 335–345 (2016). doi:10.1016/j.egypro.2016.05.044
43. W. Luo, W. Xu, Q.Y. Pan et al., A 4D Monte Carlo laser-Compton scattering simulation code for the characterization of the future energy-tunable SLEGS. Nucl. Instrum. Methods Phys. A **660**(1), 108–115 (2011). doi:10.1016/j.nima.2011.09.035
44. H. Ohgaki, S. Koda, Y. Iwasaki et al., Study on energy variable laser-Compton gamma-ray with a fixed energy electron beam. J. Nucl. Sci. Technol. **44**(5), 698–702 (2007). doi:10.1080/18811248.2007.9711858
45. W. Guo, W. Xu, J.G. Chen et al., A high intensity beam line of γ-rays up to 22 MeV energy based on Compton backscattering. Nucl. Instrum. Methods Phys. A **578**(3), 457–462 (2007). doi:10.1016/j.nima.2007.05.322
46. Y. Xu, W. Xu, Y.G. Ma et al., A new study for ^{16}O (γ, α) ^{12}C at the energies of nuclear astrophysics interest: the inverse of key nucleosynthesis reaction ^{12}C (α, γ) ^{16}O. Nucl. Instrum. Methods Phys. A **581**(3), 866–873 (2007). doi:10.1016/j.nima.2007.08.078
47. J.G. Chen, W. Xu, H.W. Wang et al., Transmutation of nuclear wastes using photonuclear reactions triggered by Compton backscattering photons at the Shanghai laser electron gamma source. Chin. Phys. C **32**(8), 677 (2008). doi:10.1088/1674-1137/32/8/019
48. M. Jiang, X. Yang, H. Xu et al., Shanghai synchrotron radiation facility. Chin. Sci. Bull. **54**(22), 4171 (2009). doi:10.1007/s11434-009-0689-y